A&A, 709, A20 (2026)
https://doi.org/10.1051/0004-6361/202555265

Astronomy & Astrophysics

Dynamical state of four open clusters

Shoucheng Wang[1,3], Jiaxin Wang[2,3,⋆], Jun Ma[3,4], Zhen-Yu Wu[3,4,⋆], and Rong Zhou[1,⋆]

[1] School of Science, Hunan Institute of Technology, Hengyang 421002, China
[2] School of Science, Chongqing University of Posts and Telecommunications, Chongqing 400065, China
[3] Key Laboratory of Optical Astronomy, National Astronomical Observatories, Chinese Academy of Sciences, Beijing 100012, China
[4] School of Astronomy and Space Science, University of Chinese Academy of Sciences, Beijing 101408, China

Received 23 April 2025 / Accepted 17 March 2026

ABSTRACT

Context. Open clusters are vital laboratories for studying stellar dynamics and evolution, with mass segregation – the preferential concentration of massive stars toward cluster cores – serving as a key indicator of internal dynamical processes. This study investigates four open clusters (NGC 7243, NGC 2301, NGC 1528, and NGC 2281; ages 100–650 Myr) using deep multicolor photometry from the Beijing-Arizona-Taiwan-Connecticut (BATC) Sky Survey, combined with *Gaia* Data Release 3 (DR3), to explore their mass functions and dynamical states.

Aims. The work seeks to characterize mass segregation patterns across spatial scales to establish its origin (primordial vs. dynamical) and to provide the first conclusive evidence of mass segregation in NGC 2281. Additionally, we analyze how cluster relaxation timescales and evolutionary stages influence their dynamical architectures.

Methods. Fundamental parameters were derived via Bayesian methods. The tidal radii were determined from the intersection of the observed cumulative mass profiles and theoretical tidal mass curves, and mass functions were analyzed through power-law fits ($\Phi(m) \propto m^{\alpha}$) performed separately for the inner (bound) and outer (tidal) regions.

Results. All clusters exhibit signs of mass segregation. However, only NGC 2281 shows a statistically significant steepening of the mass function slope in its outer tidal region, indicating significant evaporation of low-mass stars and providing the first clear evidence of strong, dynamically evolved mass segregation in this cluster. For NGC 7243, NGC 2301, and NGC 1528, the derived τ values ($\tau = \mathrm{Age}/t_{\mathrm{relax}} > 3$) suggest advanced dynamical evolution, yet their outer regions contain too few stars to robustly confirm the expected steepening of the mass function.

Key words. stars: fundamental parameters – stars: luminosity function, mass function

1. Introduction

Open clusters are gravitationally bound stellar systems formed from the collapse of a single giant molecular cloud (Kroupa 2008). Their member stars share similar ages, metallicities, and kinematic properties, making them ideal laboratories for the studies of star formation, stellar evolution, and the dynamics of stellar systems. The dynamical evolution of open clusters is influenced by complex mechanisms such as stellar escape, tidal stripping, and interactions with Galactic spiral arms or molecular clouds. These processes collectively determine the clusters' lifespans and structures: low-mass clusters are more susceptible to tidal disruption, while massive clusters may gradually evolve into globular clusters over billions of years. In addition, one important and interesting aspect in the study of open clusters is the phenomenon of mass segregation; that is, the more massive member stars in the cluster are more centrally concentrated and/or have a distinct distribution in velocity space compared to lower-mass members (Chen et al. 2007). Due to two-body relaxation, mass segregation is known as dynamical mass segregation. Through two-body relaxation, equipartition of kinetic energy among different mass groups in the cluster can be achieved (Gouliermis et al. 2004). This means that low-mass stars can attain high velocities and move away from the cluster center, leading to a higher concentration of high-mass stars toward the center of the cluster (Sharma et al. 2008). According to numerical simulations, dynamical mass segregation occurs on the cluster relaxation time (Bonnell & Davies 1998). However, the mass segregation also appears in the very young open cluster, which is younger than its relaxation time. This is known as primordial mass segregation. The primordial mass segregation can be either the signature of the initial conditions and loci or can result – at least partially – from early dynamics (Gouliermis et al. 2004, and references therein). Recent advancements, particularly the high-precision astrometric data from the *Gaia* satellite, have allowed researchers to trace the 3D motions of cluster members with unprecedented accuracy, revealing internal velocity dispersions, rotational features, and tidal tails (Wu et al. 2021; Hu et al. 2021; Zhong et al. 2022; Hao et al. 2022). These observations provide new constraints on the origins of mass segregation, including the relative contributions of dynamical relaxation versus primordial segregation.

Furthermore, comparing a cluster's initial mass function with its dynamical mass function (DMF) offers insights into star formation efficiency and the loss of low-mass stars during evolution (Kroupa 2001; Baumgardt 2003; Parmentier & Gilmore 2007). For instance, mass segregation not only manifests spatially but may also influence velocity distributions through energy equipartition – where massive stars with lower

⋆ Corresponding authors: wangjx@cqupt.edu.cn; zywu@nao.cas.cn; 913922532@qq.com

Table 1. Basic information of the four open clusters provided by WEBDA.

Object	Right ascension(2000) (deg)	Declination(2000) (deg)	log (t/yr)	[Fe/H]	$(m-M)_0$	$E(B-V)$
NGC 7243	333.783	49.898	8.058	–	9.54	0.220
NGC 2301	102.938	0.46	8.216	+0.06	9.70	0.028
NGC 1528	63.846	51.215	8.568	–	9.45	0.258
NGC 2281	102.071	41.078	8.554	+0.13	8.73	0.063

velocities tend to concentrate, while low-mass stars with higher kinetic energies, migrate to the outskirts (Khalisi et al. 2007). The alignment of these theoretical predictions with observations is critical for understanding the physical conditions during cluster formation (e.g., turbulence and magnetic fields) and refining long-term evolutionary models. Thus, systematic studies of open clusters across multiple dimensions – structure, kinematics, and mass functions – not only advance stellar dynamics but also provide key clues for galactic archaeology.

In this paper, we investigate the phenomenon of mass segregation in four open clusters: NGC 7243, NGC 2301, NGC 1528, and NGC 2281. These open clusters cover a range of ages from 100 Myr to 600 Myr. The basic information of these open clusters taken from the WEBDA database is listed in Table 1. These open clusters were studied by Frolov & Ananjevskaja (2007), Sharma et al. (2008), and Francic et al. (1989). Because of the small field of view and shallow photometry, mass functions were not examined in detail in these studies. We study these open clusters using photometry from deep observations over a large field of view. Our study is based on a consistent set of BATC observations, supplemented by member lists from *Gaia* DR3 (Hunt & Reffert 2023), which allows us to search for mass segregation in a uniform manner and to investigate the differences among the clusters concerning the phenomenon with an expanded spatial coverage. In this paper, we present multicolor photometry of these open clusters, obtained with the BATC Multicolor Survey photometric system. The BATC photometric system consists of 15 intermediate-band filters covering the 3000–10 000 Å wavelength range, designed to avoid most of the known bright and variable night-sky emission lines. This filter system is appropriate for obtaining the spectral energy distributions (SEDs) of objects. In the BATC system, an E2V 4k × 4k thinned Charge-Coupled Device (CCD) with a pixel size of 12 µm, a field of view of 94′ × 94′, and a resolution of 1.36″ pixel^{-1}(Fan et al. 2009) is used. Taking advantage of deep photometry and the BATC photometric system's large field of view, we investigate open clusters in our Galaxy. In previous work, we used photometry from the BATC photometric system to study open clusters in our Galaxy: M67 (Fan et al. 1996); M48 and NGC 7789 (Wu et al. 2005, 2006, 2007); and NGC 188 and NGC 1039 (Wang et al. 2015, 2017). In this study, we examined the dynamical state of four open clusters. For this purpose, we first derived fundamental parameters (age, metallicity, distance, and reddening) via Bayesian analysis of the multicolor photometry. Subsequently, we determined a physically motivated tidal radius (R_t) for each cluster by comparing the observed cumulative mass profile with the theoretical tidal mass curve in the Galactic potential following the method of Röser et al. (2011). Stars inside R_t were treated as bound members, while those outside were considered part of the tidal region. Finally, we constructed and compared the present-day mass functions (PDMFs) separately for the inner ($R < R_t$) and outer ($R > R_t$) regions to quantify mass segregation and assess the clusters' dynamical ages.

Table 2. Parameters of 14 BATC filters.

Number	Filter name	$\lambda_{\rm eff}$ (Å)	FWHM (Å)
1	*a*	3360	360
2	*b*	3890	340
3	*c*	4194	309
4	*d*	4540	332
5	*e*	4925	374
6	*f*	5267	344
7	*g*	5790	289
8	*h*	6074	308
9	*i*	6656	491
10	*j*	7057	238
11	*k*	7546	192
12	*m*	8023	255
13	*n*	8484	167
14	*o*	9182	247

We present our new observations and photometric data in Section 2. In Section 3, we derive the fundamental parameters of the four open clusters and derive their tidal radii and mass functions in Section 4. We provide a summary in Section 5.

2. Observation and photometric data

2.1. Observation

The observations were carried out using the BATC photometric system with the 60/90 cm f/3 Schmidt telescope at the Xinglong Station of the National Astronomical Observatories, Chinese Academy of Sciences (NAOC). More details about the BATC system are described in Yan et al. (2000). Images of open clusters observed by the BATC *o* band are shown in Fig. 1. The parameters of the BATC filters are given in Table 2. Columns 1 and 2 list the IDs and names of the BATC filters; Columns 3 and 4 list the effective wavelength and full width at half-maximum (FWHM) of each filter. The observational details for each open cluster are given in Table A.1, including the exposure time and the number of frames per filter. The typical seeing in these observations is $3\farcs6 \pm 0\farcs5$. Because the images observed in the p band are not deep enough, the photometric data of this band are not used here.

2.2. Photometric data

Photometric reduction was carried out as follows. Using the automatic data processing program, PIPELINE I (Fan et al. 1996), we preformed standard bias subtraction and field flatting.

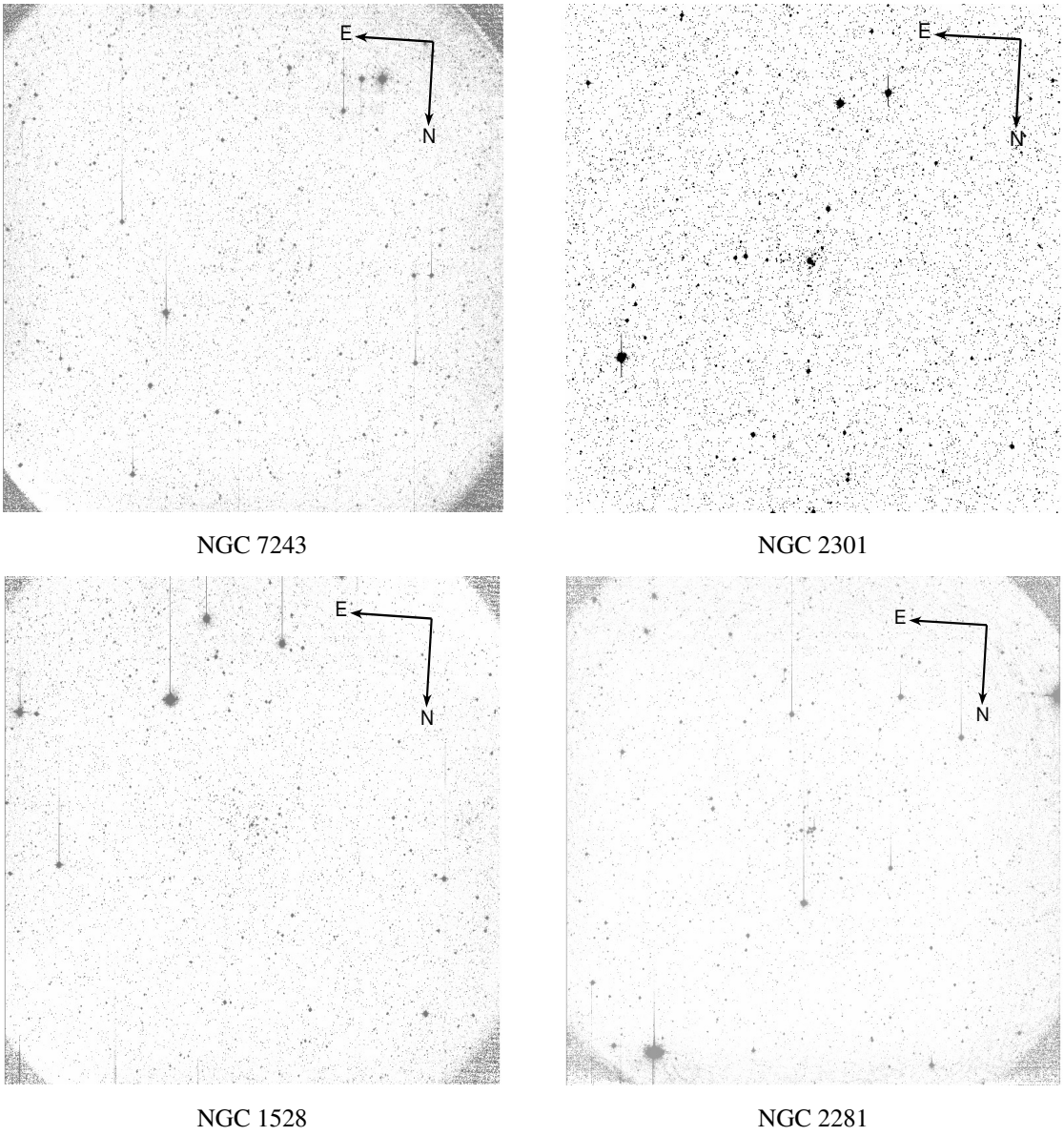

Fig. 1. BATC *o*-band images of the target open cluster regions. The field of view is 94′ × 94′.

Wide-field images typically have optical distortions that cause the point spread function (PSF) to vary across the field; therefore, the full image was divided into nine subregions. In the subregion, the PSF almost does not vary with location. Thus, we used the PIPELINE II program based on the DAOPHOT II stellar photometric reduction package of Stetson (1987) to measure the instrumental magnitudes of point sources in the subregions. Subsequently, the instrumental magnitudes $M_{\rm inst}$ were calibrated to the BATC AB magnitude $M_{\rm batc}$ (see Zhou et al. 2003; Ma et al. 2017, for details). The value of $M_{\rm batc} - M_{\rm inst}$ and the calibration error are listed in Columns 4 and 5 of Table A.1, respectively. For each star observed more than once in a BATC band, the final photometry in that band is its weighted mean.

2.3. Completeness correction

To derive the mass functions of open clusters, the completeness estimation is required. We adopted the artificial star test (see Wu et al. 2007, for details) to obtain the completeness correction. Artificial stars are generated based on the PSF and luminosity distribution of the original images and uniformly distributed across them. To avoid overcrowding, the total number of artificial stars was limited to 15% of the original number. The photometric reduction was then carried out on these test images using the same parameters and procedures as for the original images described in Section 2.2. The proportion of recovered artificial stars among all added artificial stars is defined as the completeness correction. Table A.2 lists the completeness corrections for each open cluster.

3. Fundamental parameters

3.1. Preliminary candidate cluster members

To determine the fundamental parameters of open clusters, we needed samples of preliminary candidate cluster members. We chose preliminary candidate cluster members based

Table 3. Starting values for BASE-9.

Object	Number[a]	log (t/yr)	[Fe/H]	$(m-M)_0$	$E(B-V)$
NGC 7243	550	7.97	0.00	9.65	0.22
NGC 2301	280	8.35	+0.06	9.53	0.06
NGC 1528	261	8.55	0.00	9.89	0.25
NGC 2281	155	8.79	+0.13	8.49	0.07

Notes. [a] The number of preliminary candidate cluster members.

on the membership probabilities of stars and cluster radii provided by the Milky Way Star Clusters (MWSC) catalog (Kharchenko et al. 2012, 2013). First, we cross-matched our star catalog and the MWSC catalog using a matching tolerance of 1.0″ to identify common stars. Next, we selected stars with membership probabilities higher than 61% and located within cluster radii. These stars define the stellar samples used in our subsequent analysis. Preliminary candidate cluster member counts are listed in Table 3.

3.2. Bayesian method

In general, the fundamental parameters of an open cluster can be derived by visually fitting an isochrone to observed data points on a color magnitude diagram (CMD) or color–color diagram. However, there are some problems with this method. Owing to the degeneracy between fundamental parameters such as age and metallicity, and between metallicity and reddening, we find that isochones with different fundamental parameters often fit the data points on the CMD equally well. Moreover, for multicolor photometric data, fitting isochrones to observed data points over all CMDs is further complicated. To determine the fundamental parameters objectively and precisely, we adopted the Bayesian method. The Bayesian method determines the posterior distributions of the fundamental parameters, resulting in something akin to a best fit (Jeffery et al. 2016). Based on Bayesian statistics, a sophisticated software suite, named Bayesian Analysis for Stellar Evolution with Nine Parameters (BASE-9), was developed to objectively fit our models (von Hippel et al. 2006; DeGennaro et al. 2009; van Dyk et al 2009; Stein et al. 2013). Through its web interface[1], we downloaded the BASE-9 source code and used it to derive the fundamental parameters for the open clusters studied here.

The details of Bayesian technique are described in von Hippel et al. (2006) and van Dyk et al (2009). We give a brief overview of the Bayesian technique as follows. The Bayesian technique uses the observed data and our prior knowledge of the fundamental parameters to infer their posterior distributions. According to Bayes's theorem, the posterior distribution can be obtained as follows:

$$p(\theta|x) = \frac{p(\theta)p(x|\theta)}{p(x)},$$
$$p(x) = \int p(\theta)p(x|\theta)d\theta, \quad (1)$$

where $p(\theta|x)$ is the posterior density on model parameters θ given data x, $p(\theta)$ is the prior density on the model parameters θ, and $p(x|\theta)$ is the likelihood function. A simple likelihood function adopted by von Hippel et al. (2006) is as follows:

$$p(x|\theta) = \prod_{i=1}^{N}\prod_{j=1}^{n} \frac{1}{\sqrt{2\pi\sigma_{ij}^2}}\exp\left(-\frac{[M_{ij}((m-M)_0, E(B-V)) - M_j(t,Z,m)]^2}{2\sigma_{ij}^2}\right), \quad (2)$$

where N is the total number of stars in the sample, n is the total number of observed bands for the ith star, $M_j(t,Z,m)$ is the theoretical magnitude in the jth band calculated from a theoretical isochrone model with the metallicity Z, age t, and mass m. The observed magnitude $M_{ij}((m-M)_0, E(B-V))$ and its error σ_{ij} for the ith star in the jth band refer to values corrected for the distance modulus $(m-M)_0$ and reddening $E(B-V)$. Based on this simple likelihood function, van Dyk et al (2009) developed a more complete and sophisticated likelihood function that considers field star contamination and binary systems (see van Dyk et al 2009, for details). BASE-9 adopts this complete and sophisticated likelihood function. The prior distributions on metallicity, distance modulus, and reddening are assumed to be Gaussian distributions. The prior distribution on the logarithmic age is assumed to be uniform between log (t/yr) = 6.0 and log (t/yr) = 9.9 and zero elsewhere. The prior distribution on the mass is assumed to be proportional to the Miller & Scalo (1979) initial mass function. Because $p(x)$ cannot be calculated analytically, based on the likelihood function and prior distributions, BASE-9 uses the Markov chain Monte Carlo (MCMC) algorithm (see van Dyk et al 2009, for details) to generate a sample to approximate the posterior distribution.

To perform BASE-9, we input the photometric data, the theoretical isochrones, the means and standard deviations of prior distributions, and the starting values of the fundamental parameters. We used multicolor photometric data of preliminary candidate cluster members to derive the fundamental parameters of the open cluster sample. In this study, we used the Padova theoretical isochrones in the BATC system (Marigo et al. 2008). Through an interactive web interface[2], we constructed a grid of isochrones for different ages, metallicities, photometric systems, and dust properties. We used the default models with scaled-solar abundance ratios (i.e., [α/Fe] = 0.0). In addition, the reddening $E(B-V)$ was transformed to each BATC band using the extinction coefficient derived by Chen (2000), following the procedure given in Appendix B of Schlegel et al. (1998). For the prior distribution, we adopted the MWSC catalog values for the fundamental parameters as the means of Gaussian distributions. These values are listed in Table 3. Subsequently, we set the standard deviations of Gaussian distributions as follows: σ([Fe/H]) = 0.02, $\sigma((m-M)_0)$ = 0.3,

[1] https://github.com/argiopetech/base

[2] http://stev.oapd.inaf.it/cmd

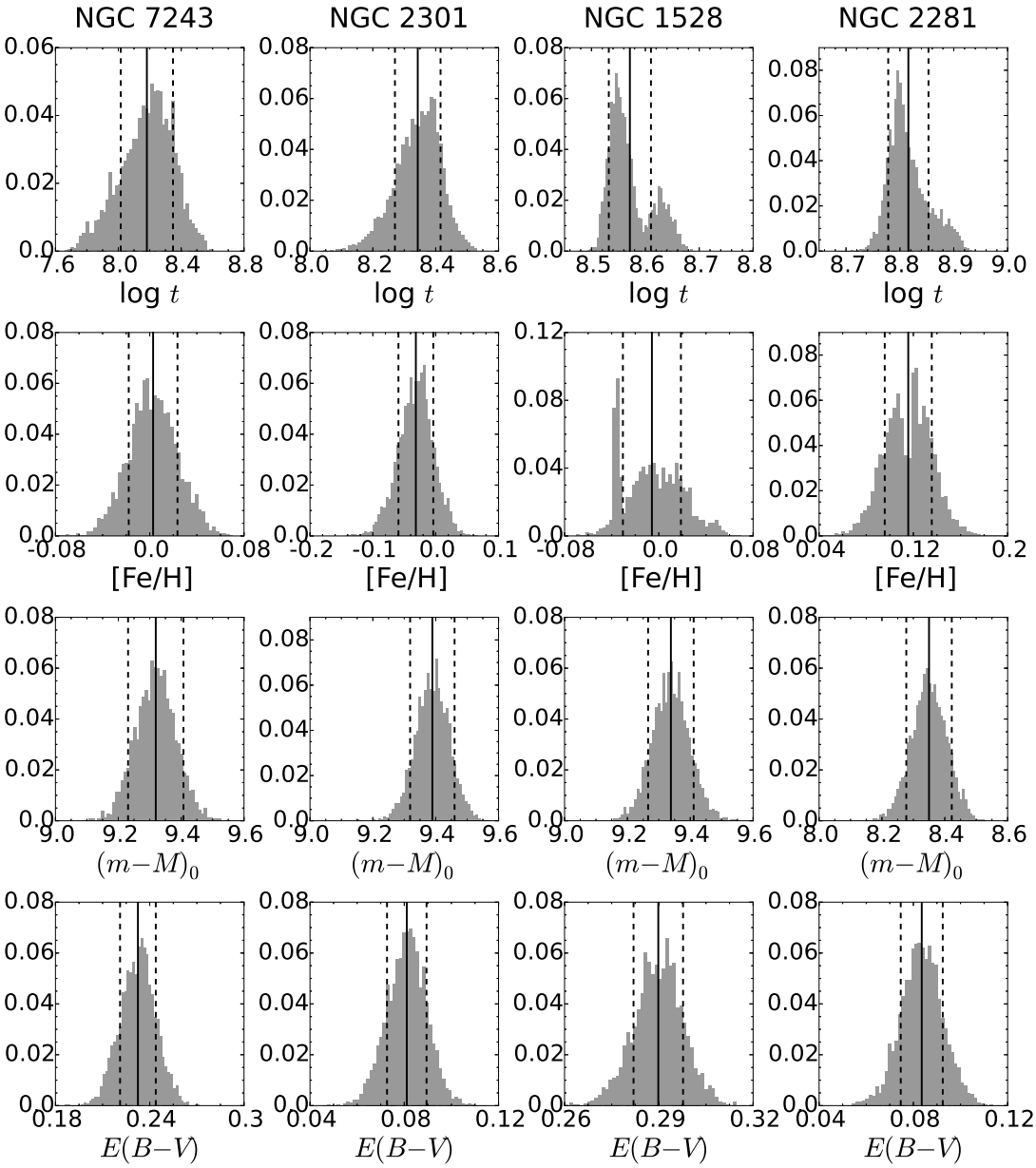

Fig. 2. All posterior distributions of the fundamental parameters. The histograms represent the posterior distributions. The perpendicular solid lines show the fundamental parameters derived from the posterior distributions. The perpendicular dashed lines show the 1 σ errors.

and $\sigma(E(B-V)) = 0.03$. For the starting values, Jeffery et al. (2016) showed that BASE-9 generates consistent results regardless of starting values. Therefore, we adopted the fundamental parameter values from the MWSC catalog as our starting point.

3.3. Result

We ran BASE-9 on each open cluster. For each open cluster, we ran the chain for 50 000 steps and used the last 20 000 steps to infer the posterior distributions. Figure 2 shows the posterior distributions of the fundamental parameters. We used the means and standard deviations of the posterior distributions to estimate the values of the fundamental parameters and their uncertainties, respectively, and list these estimates in the summary of Table 5. To check the fundamental parameters obtained here, we plot isochrones (black lines) corresponding to the Bayesian-derived parameters on the observed CMDs for each cluster. As shown in Fig. 3, these isochrones reproduce the observed data well.

We compare our results with those from the previous studies listed in Table 4. For NGC 7243, the 150^{+70}_{-50} Myr age obtained here is consistent with the 250 ± 50 Myr age obtained by Jilinski et al. (2003) and slightly greater than the 76 ± 3 Myr age obtained by Hill & Barnes (1971). Hill & Barnes (1971) argued that the 76 ± 3 Myr age is a lower limit estimation. The distance modulus and reddening of NGC 7243 derived here are consistent with those in the previous studies. For NGC 2301, the 220^{+40}_{-30} Myr age is in good agreement with the 250^{+60}_{-50} Myr age obtained by Kim et al. (2001) and slightly greater than the 160 Myr age obtained by Sharma et al. (2006). The metallicity obtained here is consistent with previously published results. However, the distance modulus is smaller than previously published results, and the reddening is greater than previously

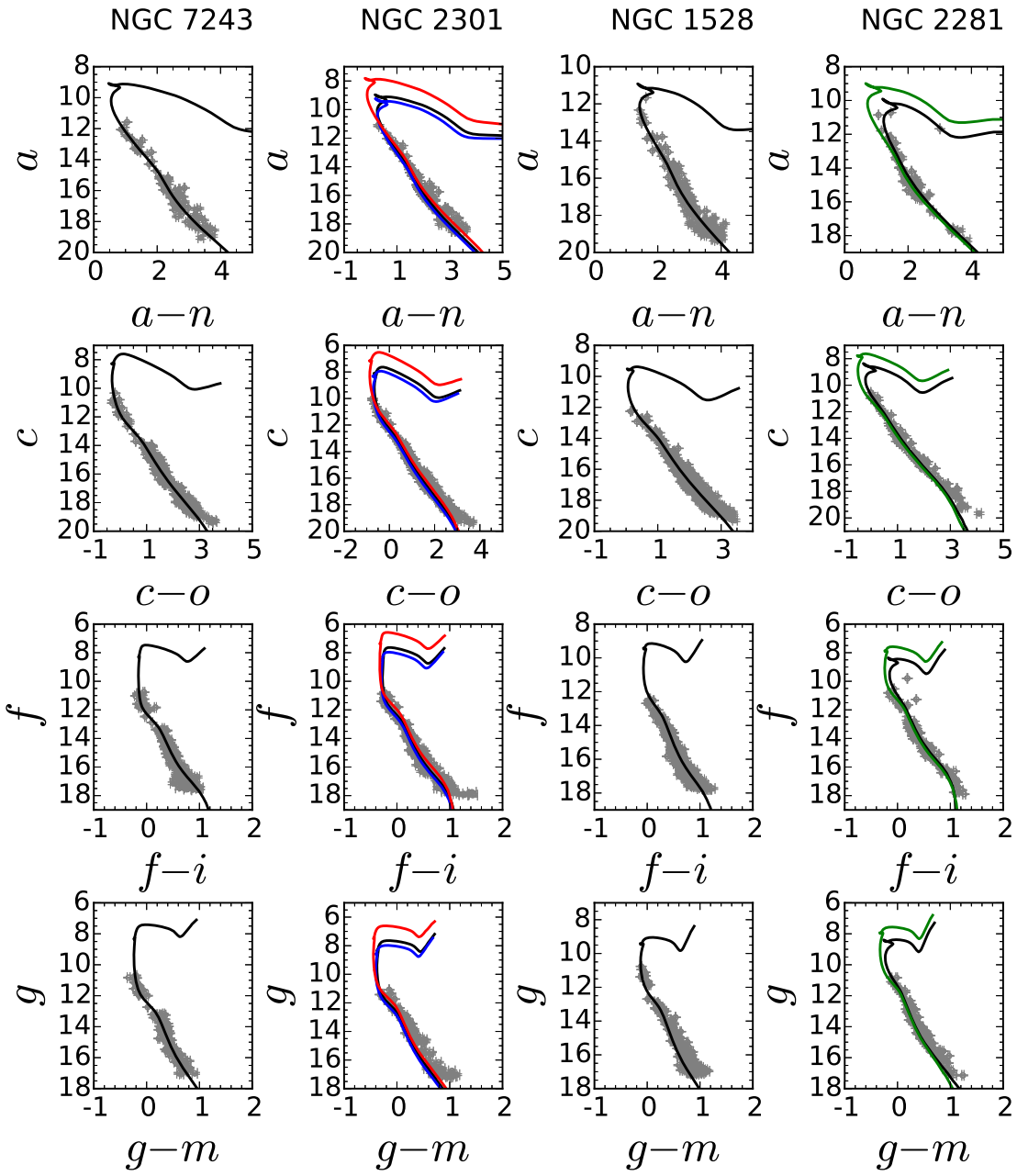

Fig. 3. Observed CMDs of open clusters, including $(a - n)$ vs. a, $(c - o)$ vs. c, $(f - i)$ vs. f, and $(g - m)$ vs. g CMDs. The circles represent preliminary candidate cluster members. Error bars represent photometric errors. The solid black lines represent BATC isochrones with the fundamental parameters derived from the Bayesian method. The solid red lines represent isochrones with the fundamental parameters derived by Sharma et al. (2006). The solid blue lines represent isochrones with the fundamental parameters derived by Kim et al. (2001). The solid green lines represent isochrones with the fundamental parameters derived by Francic et al. (1989).

published results. To check the discrepancy between our result and those from the previous studies, we plot isochrones with the fundamental parameters obtained by Kim et al. (2001) and Sharma et al. (2006) on CMDs. As shown in Figure 3, the isochrones (red lines) for the fundamental parameters derived by Sharma et al. (2006) are redder than the main-sequence data on all the CMDs, particularly in the $(a - n)$ versus a and $(f - i)$ versus f CMDs. The isochrones (blue lines) for the fundamental parameters provided by Kim et al. (2001) are bluer than the main-sequence data on all the CMDs. It is evident that our theoretical curves match the data points better than those obtained with the fundamental parameters in the previous studies. For NGC 1528, the result obtained here is consistent with the previously published results. For NGC 2281, the 650 ± 60 Myr age obtained here is greater than the 400 Myr age obtained by Francic et al. (1989). The metallicity obtained here is richer than those obtained by Francic et al. (1989) and Zhang et al. (2015). To check the discrepancy between our result and those from previous studies, we plot isochrones (green lines) with the fundamental parameters obtained by Francic et al. (1989) on CMDs. As shown in Fig. 3, the black line reproduces the data points better than the green line does on the $(a - n)$ versus a CMD. The distance modulus and reddening of NGC 2281 obtained here are consistent with those from previous studies.

Table 4. Literature estimates of fundamental parameters for the four open clusters.

Object	t	[Fe/H]	$(m-M)_0$	$E(B-V)$	Reference
NGC 7243	76 ± 3 Myr	0.00(adopted)	9.4 ± 0.1	0.24 ± 0.06	Hill & Barnes (1971)
	250 ± 50 Myr	0.00(adopted)	9.22 ± 0.37	0.24	Jilinski et al. (2003)
NGC 2301	–	0.04 ± 0.12	9.62	0.04 ± 0.02	Nissen (1988)
	–	0.06 ± 0.06	9.66	0.04	Twarog et al. (1997)
	250^{+60}_{-50} Myr	0.00(adopted)	9.6 ± 0.1	0.05 ± 0.03	Kim et al. (2001)
	160 Myr	0.00(adopted)	9.7	0.03	Sharma et al. (2006)
NGC 1528	400 Myr	−0.133	8.9	0.28	Francic et al. (1989)
	400 Myr	0.00(adopted)	10.19	0.26	Sharma et al. (2006)
	–	$-0.08^{+0.27}_{-0.19}$	–	–	Zhang et al. (2015)
NGC 2281	–	–	8.3 ± 0.83	0.07 ± 0.03	Yoshizawa (1978)
	400 Myr	−0.074	8.33	0.09	Francic et al. (1989)
	–	$-0.09^{+0.12}_{-0.18}$	–	–	Zhang et al. (2015)

Table 5. Summary of fundamental parameters and dynamical properties of the four open clusters.

Parameter	NGC 7243	NGC 2301	NGC 1528	NGC 2281
Right Ascension (J2000) (deg)	333.795	102.945	63.847	102.075
Declination (J2000) (deg)	49.875	0.465	51.19	41.08
log (t/yr)	8.18 ± 0.17	8.34 ± 0.07	8.57 ± 0.04	8.81 ± 0.04
t (Myr)	150^{+70}_{-50}	220^{+40}_{-30}	370 ± 30	650 ± 50
[Fe/H]	0.00 ± 0.02	−0.03 ± 0.03	0.00 ± 0.02	+0.12 ± 0.02
$(m-M)_0$	9.31 ± 0.09	9.39 ± 0.07	9.34 ± 0.07	8.34 ± 0.07
$E(B-V)$	0.23 ± 0.01	0.08 ± 0.01	0.29 ± 0.01	0.08 ± 0.01
Tidal radius (pc)	10.69	13.13	11.24	11.03
Tidal masses ($M_\odot$)	484	793	497	493
Number of cluster members	503	828	463	717
OC A (km s^{-1} kpc^{-1})	+15.06 ± 0.3	+14.19 ± 0.4	+14.17 ± 0.3	+14.52 ± 0.4
OC B (km s^{-1} kpc^{-1})	−13.23 ± 0.5	−12.36 ± 0.4	−12.34 ± 0.4	−12.69 ± 0.4
$t_{\rm relax}$ (Myr)[a]	35.2	66.0	34.6	49.0
τ = Age/$t_{\rm relax}$	4.26	3.34	10.7	13.3
α (Inner region)[b]	−2.48 ± 0.08	−2.61 ± 0.19	−2.14 ± 0.16	−2.63 ± 0.29
α (Outer region)[b]	−2.54 ± 0.55	−2.16 ± 0.67	−2.27 ± 0.34	−3.76 ± 0.23

Notes. [a] The relaxation time of the four open clusters. [b] Fitting parameters for the mass functions of the four open clusters.

4. Dynamical state

4.1. Tidal radius

To obtain a relatively robust and physically meaningful determination of the tidal radius for each cluster, we adopted the method described by Röser et al. (2011). This method involves comparing the observed cumulative mass profile of the cluster with the theoretical relation between tidal mass and tidal radius in the Galactic potential, with their intersection defining the tidal radius (R_t).

The central coordinates of the open cluster sample are taken from the MWSC catalog (listed in Table 5). We first constructed the observed cumulative mass profile. To obtain a relatively complete census of cluster members across a larger spatial extent, we utilized the member star catalogs from Hunt & Reffert (2023), derived from *Gaia* DR3 data using a clustering algorithm. To acquire the necessary multicolor photometry for SED fitting, we cross-matched this member list with our BATC source catalog. For stars that were successfully matched, we used their measured BATC magnitudes. However, due to the limited field of view of the BATC observations, a subset of member stars from the *Gaia*-based catalog fell outside BATC's field of view. For these unmatched stars, we directly adopted their G, $G_{\rm BP}$, and $G_{\rm RP}$ magnitudes from *Gaia* DR3 as input photometry for the subsequent analysis.

We derived the individual mass for each member star (with photometry from either BATC or *Gaia*) by performing SED fitting. The fitting procedure minimizes the χ^2 statistic, defined as

$$\chi^2 = \sum_{j=1}^{n_{\rm bands}} \frac{(m_{{\rm obs},j} - m_{{\rm model},j})^2}{\sigma_j^2}, \tag{3}$$

where $m_{{\rm obs},j}$ and σ_j are the observed magnitude and its uncertainty in the j-th photometric band (BATC or *Gaia*), respectively, and $m_{{\rm model},j}$ is the magnitude predicted by a stellar model from a theoretical isochrone of given age and metallicity (as determined in Section 3). The stellar mass corresponding to the model that yields the minimum χ^2 was adopted as the mass of the star. The cumulative mass $M_{\rm cum}(< r)$ as a function of the projected distance r from the adopted cluster center was then computed by summing the masses of all member stars within that radius.

The theoretical tidal mass profile, $M_{\rm tid}(r)$, for a cluster in the Galactic potential was computed using the formulation from

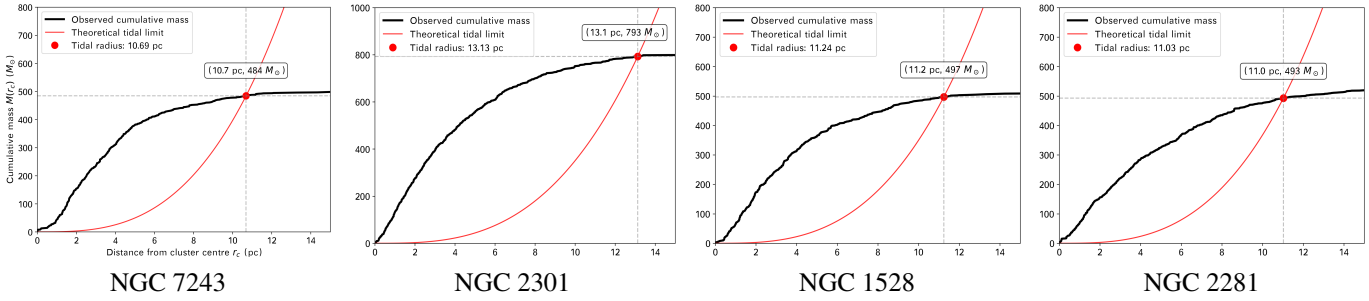

Fig. 4. Cumulated mass as a function of distance from the four cluster centers r_c. The thick black curve represents the observed cumulated mass function as obtained from adding all the individual masses within a distance r_c. The (thinner) red curve represents the relation between the tidal radius and the tidal mass in the gravitational field of the Galaxy near the position of the Sun. The red point indicates tidal radius.

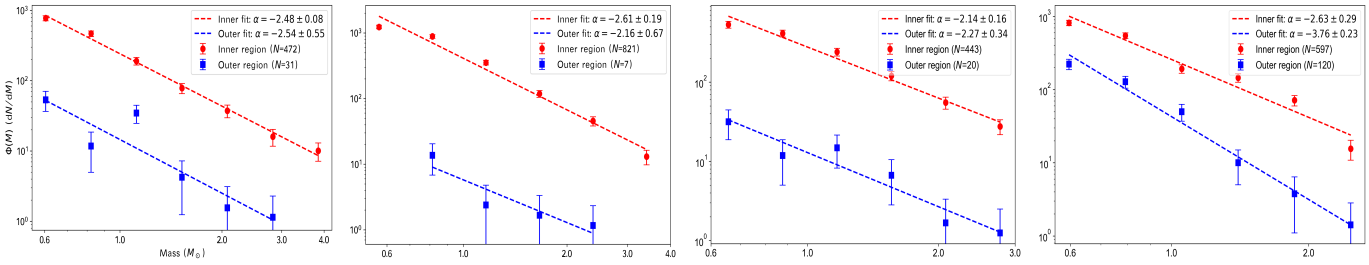

Fig. 5. Mass functions of inner ($R < R_t$) vs. outer ($R > R_t$) regions for the four open clusters. The red circles represent data points for the inner (bound) region within the tidal radius, while the blue squares represent data points for the outer (tidal) region beyond the tidal radius. The error bars indicate 1σ Poisson uncertainties. The dashed red and blue lines show the best-fit power-law functions $\Phi(M) \propto M^{\alpha}$ for the inner and outer regions, respectively. The derived slopes α and their uncertainties are given in each legend. The abscissa shows stellar mass in solar units ($M_\odot$) on a logarithmic scale with linear numerical labels; and the ordinate shows the mass function $\Phi(M) = dN/dM$ on a logarithmic scale. The number of member stars (N) in each region is indicated in the respective legend entries.

Röser et al. (2011), which depends on the local Oort constants (OC) A and B at the cluster's position. To calculate A and B, we first determined the Galactic rotational velocity $\Theta(R)$ at the Galactocentric distance R of each cluster using the recent rotation curve from Zhou et al. (2023). Subsequently, the OCs were derived using the relations given by Piskunov et al. (2006) (their Eq. (8)):

$$A = -\frac{1}{2}\left(\frac{\Theta}{R} - \frac{d\Theta}{dR}\right), \quad B = -\frac{1}{2}\left(\frac{\Theta}{R} + \frac{d\Theta}{dR}\right). \tag{4}$$

With A and B thus determined, the theoretical relation $M_{\rm tid}(r)$ was evaluated.

For each of the four clusters, we plotted the observed $M_{\rm cum}(< r)$ and the theoretical $M_{\rm tid}(r)$ on the same axes. The tidal radius R_t was then defined as the projected radius r at which these two curves intersect. The resulting plots are provided in Fig. 4, where the thick black curve represents $M_{\rm cum}(< r)$, the thinner red curve represents $M_{\rm tid}(r)$, and the intersection point (marked in red) indicates the derived R_t. These dynamically estimated tidal radii and OCs A and B are listed in Table 5. Table A.3 presents sample data for each member star in the four open clusters, including right ascension (RA) and declination (Dec), unique *Gaia* DR3 source identifier, BATC and *Gaia* photometry, and derived stellar masses. For each cluster, we assumed that all member stars share the same metallicity and age, as derived for the cluster as a whole in Table 5. The complete tables for all member stars, which contain the full set of photometric magnitudes (BATC bands *a* through *o*; *Gaia* G, BP, and RP) and initial masses, are available at the CDS.

4.2. Mass function

We now study the mass function for each cluster based on the tidal radius R_t obtained (see Sect. 4.1). Stars inside R_t are considered to be (presently) bound members, while those outside R_t are likely stars that have been stripped or are in the process of escaping. For each cluster we constructed the PDMF separately for the inner ($R < R_t$) and outer ($R > R_t$) regions. The PDMFs were derived by star counts in logarithmic mass bins and fitted with a single-segment power law $\Phi(m) \propto m^{\alpha}$ over the observed mass range. To mitigate the impact of incompleteness at the faint end, we determined the 90% completeness limit for each cluster from the artificial star tests described in Sect. 2.3, defined as the magnitude at which the completeness fraction falls below 0.9. Using the best-fitting Padova isochrones and the cluster parameters listed in Table 5, we converted these magnitude limits into mass limits. For NGC 7243, NGC 2301, NGC 1528, and NGC 2281, the corresponding mass limits are approximately 0.79 $M_\odot$, 0.74 $M_\odot$, 0.72 $M_\odot$, and 0.54 $M_\odot$, respectively. In the following analysis, all mass bins significantly below these limits, which exhibit the characteristic downturn caused by incompleteness, were excluded from the fitting procedure. The resulting mass functions for the four clusters are displayed together in Fig. 5, and the results are listed in Table 5.

In a dynamically evolving cluster, two-body relaxation drives the system toward energy equipartition. As a consequence, low-mass stars gain kinetic energy and tend to migrate to larger radii or even escape, while massive stars sink toward the center. This process naturally produces a radial gradient in the mass--function slope: the inner region becomes enriched in massive stars (flatter α), whereas the outer region (and the tidal tails)

becomes dominated by low-mass stars (steeper α). The strength of this gradient and the total number of stars outside the tidal radius are therefore key diagnostics of the cluster's dynamical age.

To quantify the expected degree of dynamical evolution, we estimated the relaxation time $t_{\rm relax}$ using the standard formula (Binney & Tremaine 2008):

$$t_{\rm relax} = \frac{N\, t_{\rm cross}}{8 \ln N},$$

where N is the number of member stars and $t_{\rm cross} = R_t/\sigma_v$ is the crossing time. We adopted a typical velocity dispersion $\sigma_v \approx 3$ km s^{-1} (Binney & Merrifield 1998) and the tidal radii R_t derived here. The resulting relaxation times and the dimensionless parameter $\tau = {\rm Age}/t_{\rm relax}$ are listed in Table 5.

According to stellar-dynamics theory, clusters with $\tau >$ 3–5 experience multiple relaxation times and should exhibit clear signatures of energy-equipartition, i.e., a steepening of the mass-function slope in the outer regions. Our derived τ values place all four clusters in this regime, yet the observed mass-function gradients show diverse patterns.

For NGC 7243 the inner region yields a slope $\alpha_{\rm in} = -2.48 \pm 0.08$ (see in Table 5), while the outer region gives $\alpha_{\rm out} = -2.54 \pm 0.55$. Although the outer slope is slightly steeper, the large uncertainty on $\alpha_{\rm out}$ (owing to the very small number of stars in the tidal region, $N_{\rm out} \sim 30$) makes the difference statistically insignificant. The global mass function, integrated over the whole field, has a slope $\alpha_{\rm global} \approx -2.5$ and shows no obvious break, remaining consistent with a Kroupa (2001)-type IMF. With $\tau \approx 4.3$, the cluster experiences several relaxation times, yet the outer PDMF does not show the predicted steepening. This discrepancy likely reflects the early phase of tidal stripping: evaporated low-mass stars have not yet accumulated sufficiently in the immediate vicinity of the cluster to alter the slope measurably, or the adopted global velocity dispersion overestimates the actual crossing time.

The case of NGC 2301 is somewhat different. Here, the inner slope is $\alpha_{\rm in} = -2.61 \pm 0.19$, and the outer slope is $\alpha_{\rm out} = -2.16 \pm 0.67$. Although the inner region shows a steeper mass function, suggesting an excess of low-mass stars in the bound region, the large uncertainty in the outer slope – stemming from the extremely small number of stars in the tidal region ($N_{\rm out} = 7$) – prevents a robust determination of the radial gradient. With $\tau \approx$ 3.3, the cluster lies at the threshold where energy-equipartition effects should become visible, but deeper photometry would be needed to confirm the expected steepening of the outer mass function.

In NGC 1528 the inner slope is $\alpha_{\rm in} = -2.14 \pm 0.16$, and the outer slope is $\alpha_{\rm out} = -2.27 \pm 0.34$. The outer region contains only $N_{\rm out} = 20$ stars, and although the outer slope is slightly steeper, the large uncertainties mean that the difference is not statistically significant. This likely reflects the poor statistics in the tidal region rather than a true mass-function gradient. Despite a large $\tau \approx 10.7$, which suggests that the cluster should have experienced significant dynamical evolution, the observed steepening in the outer region is only marginal and statistically inconclusive. This could be attributed to the fact that the tidal region has only recently begun to accumulate a detectable population of low-mass stars, and the current number remains insufficient to robustly alter the measured slope. Alternatively, the adopted velocity dispersion may overestimate the actual crossing time, leading to an overestimation of τ and the expected degree of energy equipartition.

The clearest and most robust signature of advanced dynamical evolution is seen in NGC 2281. Here, the inner region exhibits a relatively flat slope $\alpha_{\rm in} = -2.63 \pm 0.29$, while the outer region shows a much steeper slope $\alpha_{\rm out} = -3.76 \pm 0.23$. The difference is significant and is supported by a large number of stars in both regions ($N_{\rm in} \sim 600$ and $N_{\rm out} \sim 120$). With $\tau \approx 13.3$, NGC 2281 has experienced many relaxation times, allowing energy-equipartition to efficiently segregate massive stars inward and push low-mass stars outward. The steep outer PDMF directly reflects this accumulation of low-mass stars in the tidal region, providing the first conclusive evidence of strong mass segregation in this cluster.

In summary, the four clusters span a range of dynamical states. Despite their formally high τ values ($\tau \gtrsim 3$), NGC 7243, NGC 2301, and NGC 1528 show only mild or statistically ambiguous gradients in their PDMF slopes. This indicates that the simple scaling $\tau = {\rm Age}/t_{\rm relax}$ may overestimate the actual degree of energy-equipartition in these systems, possibly because of their specific orbital histories, anisotropic tidal fields, or because the evaporated low-mass stars have not yet populated the observed outer annulus in sufficient numbers. In contrast, NGC 2281 ($\tau \approx 13.3$) exhibits a clear, statistically significant steepening of the mass function in the tidal region – unambiguous evidence that energy-equipartition has substantially altered the mass-function shape and that the cluster is in an advanced state of dynamical evolution.

4.3. Spatial distribution

To visually examine the internal and external structure of the four clusters, we constructed 2D spatial distribution maps in physical units. Figure 6 shows the projected positions of all member stars for each cluster, with the cluster center at the origin $(0, 0)$. Bound members (located within the tidal radius R_t) are shown in blue, while stars in the tidal region ($r \geq R_t$) are shown in red. The dashed gray circle in each panel indicates the tidal radius determined in Section 4.1.

The projected coordinates (X, Y) in parsecs were derived from the celestial coordinates of each member star as follows. First, the angular offsets in right ascension and declination ($\Delta\alpha$, $\Delta\delta$) relative to the cluster center were computed. These angular offsets were then converted to physical projected distances using the cluster distance d (derived from the distance modulus in Section 3.3). Specifically, the projected X and Y coordinates were calculated as

$$X_{\rm pc} = d \cdot (\Delta\alpha \cos\delta_0)_{\rm rad}, \quad (5)$$

$$Y_{\rm pc} = d \cdot (\Delta\delta)_{\rm rad}, \quad (6)$$

where δ_0 is the declination of the cluster center and the subscript "rad" indicates the angular offsets expressed in radians. The conversion from angular to linear scale accounts for the $\cos\delta_0$ factor to properly scale right ascension offsets.

As shown in Fig. 6, all four clusters exhibit clear mass segregation, with more massive stars (not shown in this figure but evident from the mass functions) concentrated toward the center. The spatial distributions also reveal the extent of each cluster's tidal region, with NGC 2281 showing the most extended structure.

5. Summary

In this paper, we presented the multicolor photometric data of four open clusters observed by the BATC system. Based on these

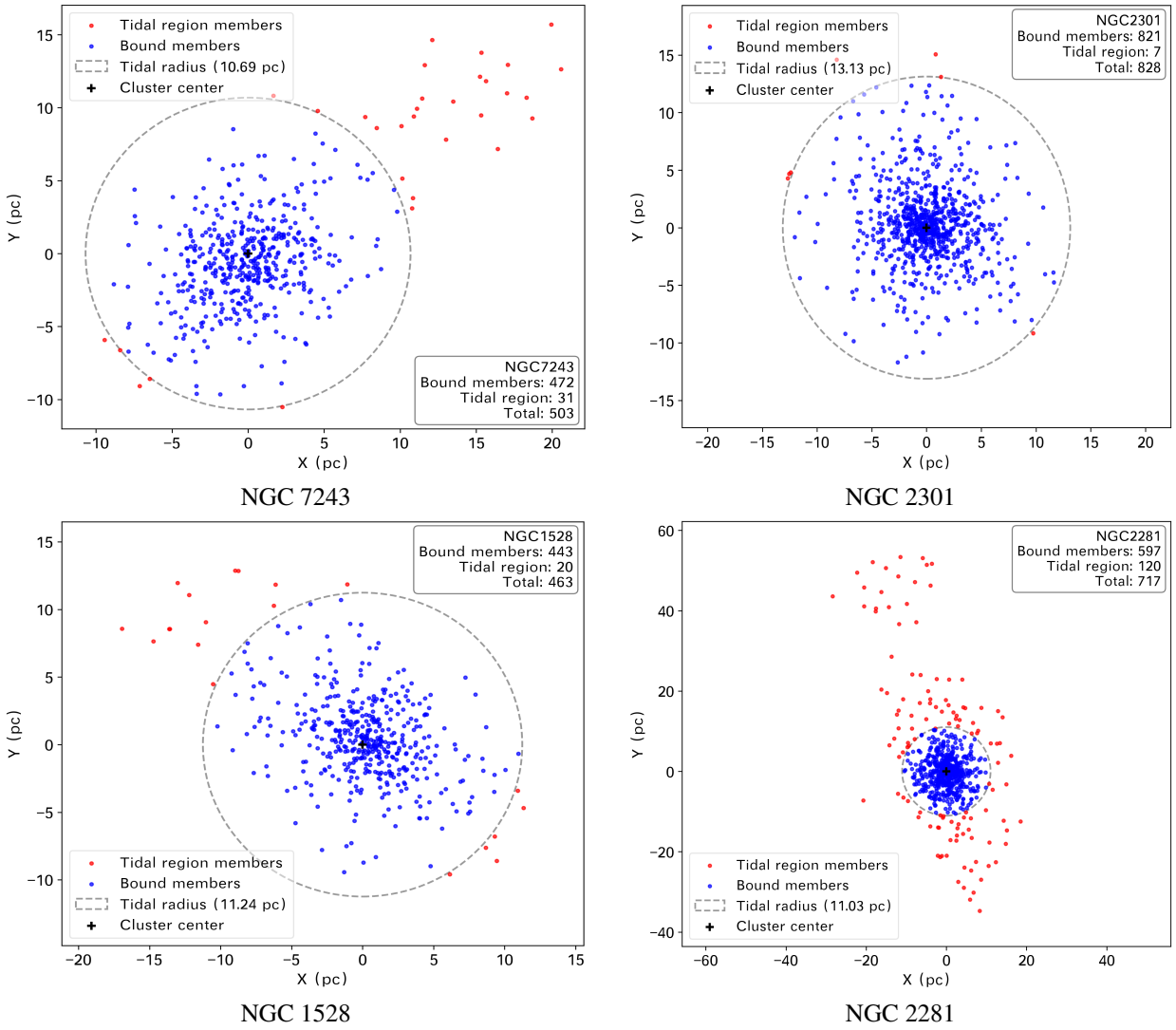

Fig. 6. Spatial distribution of member stars in the four open clusters. The projected positions are shown in parsecs relative to the cluster center at $(0, 0)$. The blue points represent stars within the tidal radius (bound members), while the red points represent stars in the tidal region ($r \geq R_t$). The dashed gray circle in each panel indicates the tidal radius R_t derived in Section 4.1. All clusters show central concentrations and extended distributions of members in the tidal region, particularly evident for NGC 2281. The spatial distributions were constructed using member lists from Hunt & Reffert (2023) and projected distances calculated from Gaia DR3 positions and cluster distances ($E(B-V)$) from Table 5.

photometric data, we adopted the Bayesian method to derive the fundamental parameters of these open clusters. The photometric data were supplemented by *Gaia* DR3 photometry for member stars outside the BATC footprint.

We determined the tidal radius R_t for each cluster using a dynamical method based on the intersection of the observed cumulative stellar mass profile and the theoretical tidal mass curve. This method provides a physically motivated definition of the cluster boundary. Stars inside R_t are considered bound members, while those outside are likely escaping or have already been stripped. We then constructed the PDMFs separately for the inner ($R < R_t$) and outer ($R > R_t$) regions. The mass functions were fitted with a single-segment power law $\Phi(m) \propto m^{\alpha}$.

Our analysis reveals that all four clusters show indications of mass segregation, but with varying degrees of statistical robustness. For NGC 7243, NGC 2301, and NGC 1528, the outer regions contain very few stars, leading to large uncertainties in the outer mass function slopes. Although their dimensionless evolution parameters τ are large ($\tau \gtrsim 3$), suggesting multiple relaxation timescales, the expected steepening of the outer mass function is not conclusively observed, likely due to the early phase of tidal stripping or specific orbital conditions.

In contrast, NGC 2281 exhibits a clear and statistically significant difference between the inner and outer mass function slopes ($\alpha_{\rm in} = -2.63 \pm 0.29$, $\alpha_{\rm out} = -3.76 \pm 0.23$), with a substantial number of stars in both regions. With $\tau \approx 13.3$, this cluster has undergone extensive dynamical evolution, leading to efficient energy equipartition and strong mass segregation, and indicating significant loss of low-mass stars. This work provides the first conclusive evidence of advanced dynamical mass segregation in NGC 2281.

The spatial distribution maps in physical units visually confirm the concentration of bound members within the tidal radius and the extended distributions in the tidal regions, particularly for NGC 2281. Our study demonstrates the importance of combining deep, wide-field photometry with *Gaia* data and dynamical tidal radius estimates to robustly assess the mass segregation state and dynamical age of open clusters.

Data availability

Full Table A.3 is available at the CDS via https://cdsarc.cds.unistra.fr/viz-bin/cat/J/A+A/709/A20.

Acknowledgements. We are indebted to the referee for his/her thoughtful comments and insightful suggestions that improved this paper greatly. We thank Prof. Bingqiu Chen for thoughtful discussions. We acknowledge the support from the National Natural Science Foundation of China (NSFC) through grants Nos. 12203010, 12273068.

References

Baumgardt, H. 2003, IAU Joint Discussion, Evolution of Star Clusters in Tidal Fields, 25, E38
Binney, J., & Merrifield, M. 1998, in Galactic Astronomy (Princeton, NJ: Princeton University Press), Princeton Series in Astrophysics, QB857.B522
Binney, J., & Tremaine, S. 2008, in Galactic Dynamics (Princeton, NJ: Princeton University Press)
Bonatto, C., & Bica E. 2005, A&A, 437, 483
Bonnell, I. A., & Davies, M. B. 1998, MNRAS, 295, 691
Chen, A. 2000, Ph.D. thesis, Natl. Cent. Univ.
Chen, L., de Grijs, R., & Zhao, J. L. 2007, AJ, 134, 1368
DeGennaro, S., von Hippel, T., Jefferys, W. H., 2009, ApJ, 696, 12
Fan, X., et al. 1996, AJ, 112, 628
Fan, Z., Ma, J., & Zhou, X. 2009, RAA, 9, 993
Francic, S. P. 1989, AJ, 98, 888
Frolov, V. H., & Ananjevskaja, Yu. K. 2007, AstL, 33, 649
Gouliermis, D., Keller, S. C., Kontizas, E., & Bellas-Velidis, I. 2004, A&A, 416, 137
Hao, C. J., Xu, Y., Wu, Z. Y., et al. 2022, A&A, 660, A4
Hill, G., & Barnes, J. V. 1971, AJ, 76, 110
Hu, Q., Zhang, Y., & Esamdin, A. 2021, A&A, 656, A49
Hunt, E. L., & Reffert, S. 2023, A&A, 673, A114
Jeffery, E. J., von Hippel, T., van Dyk, D. A., et al. 2016, ApJ, 828, 79
Jilinski, E. G., Frolov, V. N., Ananjevskaja, J. K., Straume, J., & Drake, N. A. 2003, A&A, 401, 531
Khalisi, E., Amaro-Seoane, P., & Spurzem, R. 2007, MNRAS, 374, 703
Kharchenko, N. V., Piskunov, A. E., Röser, S., Schilbach, E., & Scholz, R. D. 2005, A&A, 438, 1163
Kharchenko, N. V., Piskunov, A. E., Schilbach, E., Röser, S., & Scholz, R.-D. 2012, A&A, 543, A156
Kharchenko, N. V., Piskunov, A. E., Schilbach, E., Röser, S., & Scholz, R. D. 2013, A&A, 558, A53
Kim, S.-L., Chun, M.-Y., Park, B.-G., et al. 2001, A&A, 371, 571
Kroupa, P. 2001, MNRAS, 322, 231
Kroupa, P. 2008, Proc. Int. Astron. Union, 3
Ma, J., et al. 2017, MNRAS, 468, 4513
Marigo, P., Girardi, L., Bressan, A., et al. 2008, A&A, 482, 883
Miller, G. E., & Scalo, J. M. 1979, ApJS, 41, 513
Nilakshi Sagar, R., Pandey, A. K., & Mohan, V. 2002, A&A, 383, 153
Nissen, P. E. 1988, A&A, 199, 146
Parmentier, G., & Gilmore, G. 2007, MNRAS, 377, 352
Piskunov, A. E., Kharchenko, N. V., Röser, S., Schilbach, E., & Scholz, R.-D. 2006, A&A, 445, 545
Röser, S., Schilbach, E., Piskunov, A. E., Kharchenko, N. V., & Scholz, R.-D. 2011, A&A, 531, A92
Schlegel, D. J., Finkbeiner, D. P., & Davis, M. 1998, ApJ, 500, 525
Sharma, S., Pandey, A. K., Ogura, K., et al. 2006, AJ, 132, 1669
Sharma, S., Pandey, A. K., Ogura, K., et al. 2008, AJ, 135, 1934
Stein, N., van Dyk, D. A., von Hippel, T., et al. 2013, Statist. Anal. Data Mining, 6, 34
Stetson, P. B. 1987, PASP, 99, 191
Twarog, B. A., Ashman, K. M., & Anthony-Twarog, B. J. 1997, AJ, 114, 2556
van Dyk, D. A., DeGennaro, S., Stein, N., Jefferys, W. H., & von Hippel, T. 2009, AnApS, 3, 117
von Hippel, T., Jefferys, W. H., Scott, J., et al. 2006, ApJ, 645, 1436
Wang, J.-X., Ma, J., Wu, Z.-Y., Wang, S., & Zhou, X. 2015, AJ, 150, 61
Wang, J.-X., Ma, J., Wu, Z.-Y., & Zhou, X. 2017, PASP, 129, 114101
Wu, Z.-Y., Zhou, X., Ma, J., Jiang, Z.-J., & Chen, J.-S. 2005, PASP, 117, 32
Wu, Z.-Y., Zhou, X., Ma, J., Jiang, Z.-J., & Chen, J.-S. 2006, PASP, 118, 1104
Wu, Z.-Y., Zhou, X., Ma, J., et al. 2007, AJ, 133, 2061
Wu, Y., Xiang, M., Chen, Y., et al. 2021, MNRAS, 501, 4, 4917
Yan, H., et al. 2000, PASP, 112, 691
Yoshizawa, M. 1978, PASJ, 30, 123
Zhang, B., et al. 2015, RAA, 8, 1197
Zhong, J., Chen, L., Jiang, Y., et al. 2022, AJ, 164, 54
Zhou, X., Jiang, Z., Ma, J., et al. 2003, A&A, 397, 361
Zhou, Y., Li, X., Huang, Y., & Zhang, H. 2023, ApJ, 946, 73

Appendix A: Additional tables

Table A.1. Statistics of observations for the four open clusters.

Object	Filter name	Exposure (s)	Number of images	$M_{batc} - M_{inst}$	Calibration error
NGC 7243.....	*a*	2460	4	−0.676	0.001
	b	2220	5	0.218	0.014
	c	2220	4	0.805	0.004
	e	1890	3	1.307	0.008
	f	360	2	1.112	0.004
	g	1560	3	0.929	0.004
	h	360	2	0.890	0.005
	i	30	1	0.767	0.013
	k	90	1	−0.193	0.008
	m	300	1	0.002	0.003
	n	2280	4	−0.941	0.002
	o	2280	4	−1.208	0.004
NGC 2301.....	*a*	1980	3	−0.998	0.001
	b	2460	4	0.075	0.016
	c	3420	5	0.693	0.004
	d	390	2	0.968	0.004
	e	390	2	1.088	0.005
	f	60	1	1.038	0.004
	g	60	1	0.867	0.004
	h	960	3	0.831	0.005
	i	30	1	0.731	0.013
	j	960	3	−0.048	0.006
	k	1590	3	−0.226	0.008
	m	1080	3	−0.187	0.004
	n	1380	4	−1.021	0.007
	o	5040	9	−1.240	0.004
NGC 1528.....	*a*	1980	3	−0.624	0.001
	b	1920	4	0.246	0.012
	c	300	1	0.820	0.004
	d	1590	5	1.005	0.008
	e	2490	5	1.119	0.004
	f	360	2	1.124	0.004
	g	1560	3	0.937	0.004
	h	1920	7	0.899	0.005
	i	180	1	0.495	0.010
	j	660	3	0.007	0.008
	k	390	2	−0.202	0.008
	m	2580	5	−0.156	0.010
	n	3180	7	−0.933	0.002
	o	1380	4	−1.209	0.004
NGC 2281.....	*a*	480	1	−0.913	0.006
	b	3420	6	0.253	0.012
	c	2520	5	0.818	0.004
	d	2100	3	1.007	0.008
	e	2190	4	1.119	0.004
	f	1260	3	0.889	0.005
	g	3420	7	0.712	0.012
	h	1560	5	0.723	0.001
	i	1110	4	0.791	0.013
	j	1560	5	0.004	0.008
	k	2490	6	−0.362	0.009
	m	2580	5	−0.152	0.010
	n	3180	7	−1.005	0.007
	o	2280	4	−1.212	0.004

Table A.2. Completeness analysis results of the four open clusters.

Object	Magnitude (mag)	$0' \leq r < 45'$
NGC 7243.....	$10 \leq e < 11$	0.533
	$11 \leq e < 12$	0.754
	$12 \leq e < 13$	0.978
	$13 \leq e < 14$	0.994
	$14 \leq e < 15$	0.991
	$15 \leq e < 16$	0.977
	$16 \leq e < 17$	0.968
	$17 \leq e < 18$	0.875
	$18 \leq e < 19$	0.394
NGC 2301.....	$10 \leq c < 11$	0.275
	$11 \leq c < 12$	0.568
	$12 \leq c < 13$	0.984
	$13 \leq c < 14$	0.991
	$14 \leq c < 15$	0.987
	$15 \leq c < 16$	0.985
	$16 \leq c < 17$	0.974
	$17 \leq c < 18$	0.906
	$18 \leq c < 19$	0.724
	$19 \leq c < 20$	0.371
NGC 1528.....	$10 \leq e < 11$	0.180
	$11 \leq e < 12$	0.389
	$12 \leq e < 13$	0.752
	$13 \leq e < 14$	0.980
	$14 \leq e < 15$	0.994
	$15 \leq e < 16$	0.987
	$16 \leq e < 17$	0.983
	$17 \leq e < 18$	0.962
	$18 \leq e < 19$	0.799
	$19 \leq e < 20$	0.501
NGC 2281.....	$11 \leq e < 12$	0.432
	$12 \leq e < 13$	0.725
	$13 \leq e < 14$	0.959
	$14 \leq e < 15$	0.984
	$15 \leq e < 16$	0.989
	$16 \leq e < 17$	0.984
	$17 \leq e < 18$	0.977
	$18 \leq e < 19$	0.946
	$19 \leq e < 20$	0.733

Table A.3. Example data table for member stars of the four open clusters.

Cluster	RA (deg)	Dec (deg)	*Gaia* DR3 Source ID	*a* mag	···	G mag	···	Mass ($M_\odot$)
NGC 7243	333.837	49.899	1999983067933729664	16.21		14.15		1.20
NGC 7243	333.757	49.903	1999981796623387136	15.27		13.27		1.40
NGC 7243	333.813	49.838	1999978223210646528	14.77		12.80		1.55
⋮								
NGC 2301	102.946	0.451	3113575969318893440	16.67		14.56		1.05
NGC 2301	102.933	0.471	3113576725234412416	10.97		10.15		2.95
NGC 2301	102.931	0.470	3113576720935499904	13.95		12.42		1.60
⋮								
NGC 1528	63.843	51.190	271668402446212480	11.68		9.90		2.98
NGC 1528	63.837	51.196	271668402446210816	13.30		11.55		2.33
NGC 1528	63.856	51.203	271669879914956288	12.57		10.92		2.62
⋮								
NGC 2281	102.062	41.072	9514796743419065 60	11.69		8.68		2.70
NGC 2281	102.089	41.085	9514811131549656 32	12.01		10.47		2.00
NGC 2281	102.030	41.077	9514799148600775 68	12.19		10.53		1.99

Notes. Columns (1): cluster name. Columns (2) and (3): right ascension and declination (J2000). Column (4): unique Gaia DR3 source identifier. Columns (5)–...: BATC magnitudes in various bands. Columns ...: *Gaia* G, BP, RP magnitudes. Last column: stellar mass derived from SED fitting. Stars in the BATC catalog are uniquely identified by celestial coordinates (RA, Dec). The complete tables for all member stars are available at the CDS.